Distribution of excitation energy in the 505 MeV $^{56}Fe+^{165}Ho$ reaction

D. R. Benton,* H. Breuer, and F. Khazaie†
Department of Physics, University of Maryland, College Park, Maryland 20742

K. Kwiatkowski and V. E. Viola
Department of Chemistry and Indiana University Cyclotron Facility, Indiana University, Bloomington, Indiana 47405

S. Bradley, A. C. Mignerey, and A. P. Weston-Dawkes
Department of Chemistry, University of Maryland, College Park, Maryland 20742
(Received 7 March 1988)

The projectile-like fragment excitation energy in the $^{56}Fe+^{165}Ho$ reaction at 9 MeV/nucleon has been obtained by applying a light particle evaporation calculation to data obtained from coincidence measurements of projectile-like and target-like fragments. It is found that the excitation energy per nucleon is greater for the projectile-like fragment than for the target-like fragment at energy losses less than 200 MeV and that the excitation energy per nucleon is shifted increasingly toward the target-like fragment as a function of increasing energy loss. This shift is found to depend strongly upon the net amount and direction of mass exchange. The variance of the excitation energy about the mean value was also obtained with the result that this variation is approximately a constant fraction of the total excitation energy above an energy loss of 75 MeV.

I. INTRODUCTION

The question of the distribution of internal excitation energy during or immediately after a damped heavy-ion collision has been of great interest for a number of years. The excitation energy distribution is an important piece of information which is needed along with the mass and charge distributions before damped collisions can be completely understood. This body of information will help shed some light on basic considerations such as the interaction between excitation energy, statistical processes, and Coulomb and nuclear forces in nuclei at these energies. Theoretical models of these collisions need this information either as input to the calculations or as a constraint on the results. In addition to these purely theoretical considerations, the resolution of this question is necessary before complete knowledge about the primary reaction fragments can be obtained. The identity of these fragments is obscured by the emission of light particles from the highly excited fragments long after the reaction between the projectile and target nuclei has ceased. Information about the excitation energy residing in each reaction fragment is a necessary component to the reconstruction of these primary fragment distributions.

A number of experiments have been performed[1-16] to determine the excitation energy division for a variety of reactions. Some of these have used two fragment coincidences to determine the kinematics of the primary reaction,[2,3] while others have detected the neutrons emitted from the fragments, sometimes in a single fragment detection experiment[1] and sometimes in an experiment measuring the coincidences between fragments.[4-7] Some of the more recent results have been based on calculations of the evaporation of light particles from the reaction fragments.[9,11] There has also been an experiment based on the mass distribution of fission fragments.[8] The earlier experiments, based on kinematic coincidence or neutron measurements, were interpreted as meaning that the excitation energy per nucleon is the same for both fragments at all values of energy loss.[1-4,6,7] On the other hand, the more recent methods have yielded results which seem to show that, at least at low energy losses, the excitation energy per nucleon is larger in the lighter fragment than in the heavier fragment.[8,9,11-13] This paper will present data from an experiment[17,18] in an attempt to explicitly resolve this apparent discrepancy and to give more quantitative results.

II. EXPERIMENTAL PROCEDURE

An experiment to determine the division of excitation energy between the projectile-like and target-like fragments in the $^{56}Fe+^{165}Ho$ reaction was performed at the Super-HILAC at Lawrence Berkeley Laboratory. A beam of 505-MeV ^{56}Fe ions was used to bombard a 200-$\mu g/cm^2$ ^{165}Ho foil supported by a 100-$\mu g/cm^2$ carbon backing. This particular beam and target combination was used because (1) previous experiments have documented this reaction well,[1,19,20] (2) both projectile and target have enough nucleons so that the system can be treated statistically, (3) there is a large mass asymmetry between projectile and target, and (4) the target does not fission easily. A 15-kV potential was applied to the target to suppress emission of electrons produced by the interaction of the beam and target. The beam current varied between 100 and 600 electronic nA and the beam spot was approximately 6 mm in diameter.

Both the projectile-like fragment (PLF), defined as the lighter reaction fragment, and the target-like fragment

(TLF), defined as the heavier fragment, were detected in coincidence in the present experiment. Figure 1 gives an overview of the experimental setup. The telescope designed to detect the PLF consisted of a system to collect parameters which allow the determination of the mass, charge, kinetic energy, and scattering angle simultaneously.[21] The time of flight of the PLF's was measured using two microchannel plate timing detectors[21,22] which were separated by a distance of 895 mm. An (8×12)-mm aperture covered with a 110-μg/cm^2 Ni foil was placed 40 mm from the target and 200 mm in front of the first channel plate to guard against low-energy photons from the target. In addition, two pairs of Sm-Co magnets were placed behind the Ni foil with their fields opposite to each other to reduce electrons produced in the target (but at the same time minimizing the deflection of heavy ions). A 19-mm diameter antiscattering aperture was placed 79 mm behind the first channel plate detector to reduce the number of particles scattering into the PLF arm.

A two-element x-y position-sensitive gas-ionization chamber[21] (GIC) was located 140 mm behind the second channel plate detector to determine the kinetic energy, charge, and scattering angle of the PLF. Isobutane at 38.5 torr was used in the chamber. The energy loss in each section (approximately 120-mm long) was in the range of 10–70 MeV. The position of the particle track through the chamber was found from the drift times of the ions in both sections of the chamber (which were mutually perpendicular to measure the position both in and out of the scattering plane). The position sensitivity was calibrated using an electropolished stainless steel grid mounted in front of the GIC during a calibration run. A silicon surface-barrier detector with an area of 400 mm^2 and sensitive depth >60 μm was mounted in the rear of the chamber to measure the residual kinetic energy of the nucleus. At the entrance window (90 μg/cm^2 polypropylene) to the GIC, an electropolished aperture of 18-mm diameter limited the angular acceptance of the PLF arm to 0.18 msr. For the data presented here, the PLF arm was centered at an angle of $+26°$ in the laboratory frame. The target was tilted $-30°$ from the beam direction away from the PLF arm to minimize the target thickness along the paths of the slow recoil fragments.

The target-like fragments were detected by an x-y position-sensitive parallel-plate avalanche counter[23] with an active width of 107 mm and an active height of 117 mm. The front of this detector was placed 276 mm from the target. This location gave the detector an angular width of 22° in (and $\pm 10°$ out of) the reaction plane. The avalanche counter was sensitive to both the in-plane and out-of-plane directions. Isobutane at 10 torr was used in the detector. The avalanche counter was calibrated using the elastic peak (for the absolute angle) and the location of the position wires inside the counter (for the size of the detector). The parallel-plate avalanche counter was set at several overlapping angles covering a range from $-32°$ to $-84°$ in the laboratory on the opposite side of the beam from the PLF arm. This range of in-plane angles, when combined with the size of the detector out-of-plane, covers most of the angular distribution of recoil particles for PLF's with a fixed angle of $+26°$.

An event was recorded if energy signals from both ΔE sections of the GIC and from the silicon detector were present. After being digitized, the nonzero parameters were written to magnetic tape. A maximum of 20 different pulse heights were written to tape with each event. These included elapsed times between various signals from the avalanche counter and from the elements in the PLF arm as well as pulse heights from the GIC, the silicon detector, and the TLF avalanche counter. Of these parameters only seven were used in the final analysis presented in this paper. These were pulse heights from both sections of the GIC and from the silicon detector, drift times (positions) from both sections of the chamber, time-of-flight between the two channel plate detectors, and the in-plane position from the TLF avalanche counter. Several of the remaining parameters were used to check the consistency of the data and the acceptance of the recoil detector.

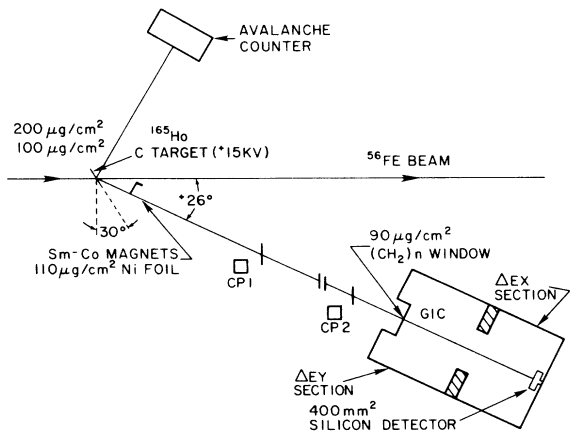

FIG. 1. Schematic of the Experiment. CP1 and CP2 are the two microchannel plate detectors, and GIC denotes the x-y position-sensitive gas-ionization chamber.

III. DATA REDUCTION

In the analysis of the present data the measured quantities for each individual event were converted into the quantities of interest, e.g., the fragment masses, charges, and excitation energies. Only in the last step were the desired *average* quantities extracted from the total of the events taken. It is evident that any experimental resolution effects and assumptions made will result in considerable uncertainties for an individual event. Examples are the determination of the intrinsically integer fragment charge derived from the energy loss in the GIC or the primary recoil angle which is modified after the reaction by the definite, but for the specific event unknown, recoil momentum due to particle evaporation.

Taking, in the final step, the average result for all events by projecting the complete data set onto one specific variable will eliminate most of the uncertainties inherent in the individual event due to the repetitive measurement of the same parameter. For many quantities of

interest the uncertainties are symmetric about a mean value (e.g., charge centroid, recoil angle), for others such as the variances, systematic deviations are obtained, which can be extracted quantitatively by observing the results for known experimental quantities (e.g., elastic scattering data) or via simulation with Monte Carlo methods. Such systematic deviations can then be corrected. The advantage of keeping event-by-event information to the latest possible stage of the analysis is that all correlations and *anticorrelations* between uncertainties are retained until the final moment, yielding the smallest possible uncertainties as well as the largest transparency about the consequences of assumptions and experimental uncertainties.

The methods used to extract the quantities of interest discussed in Secs. IV and V as well as in previous paper[17] are described in this section. Further details can be found in the Appendix and in Ref. 18.

A. Calibrations and corrections

1. Gas-ionization chamber and time-of-flight corrections

Possible nonlinearities in the electronics were investigated by taking runs before and after the experiment where a precision pulser was introduced in place of the energy signals and a time calibrator was used to simulate the inputs to the time-to-amplitude converters (TAC's). The pulse height of the pulser and the delay between signals of the time calibrator were varied by discrete amounts so that the full range of the analog-to-digital converters (ADC's) for each event was filled. These runs showed that the ADC was nonlinear near its extreme upper and lower limits. The ADC and TAC nonlinearities were corrected by using a polynomial fit to the pulser calibration.

It was found also that the time-of-flight signals from the microchannel plate detectors and energy loss signals from the ΔE sections of the GIC depended significantly on position. These discrepancies were corrected by observing the dependence of the data (pulse height and time of flight) for elastically scattered ^{56}Fe nuclei on position.

Position dependencies in the ΔE pulse heights can arise from a combination of incomplete charge collection in the GIC and chamber window deformation. Because these imperfections cause a complicated dependence of pulse height on position, the ΔE nonlinearities were corrected using the observed deviations from the expected results for the elastic events rather than by some type of calculation.

The time of flight between the channel plates in the PLF arm had similar position dependencies. The observed elastic position dependence can be seen in Fig. 2. The variation of elastic times of flight is of the order of 200 ps. This structure was presumably caused by the difference in times of flight between secondary electrons passing nearer and farther away from acceleration grid wires. Because of the finite size of the beam spot, only the second channel plate detector projects a position dependence on the PLF position in the GIC. After correcting the time of flight for the 30° tilt of the channel plate carbon foils, the average raw value of the time of flight was used to correct each event additively bin by bin in the same manner as for the ΔE pulse heights. A detailed description of the procedures can be found in Ref. 18.

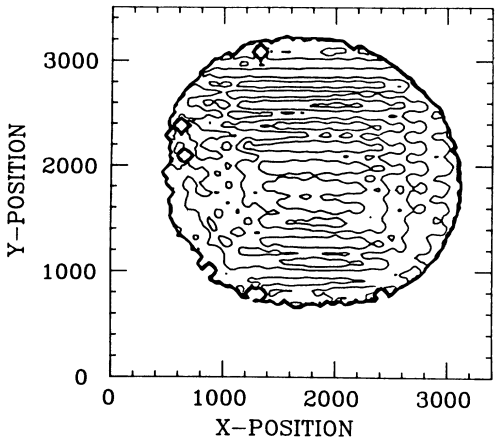

FIG. 2. Elastic time-of-flight (TOF) centroid dependence on position. The axes represent the in-plane (x) and out-of-plane (y) positions (in arbitrary units) of the PLF fragments in the GIC. The contour lines represent values of the TOF centroid. The difference between the highest and lowest contour lines on this diagram is about 500 ps. The data shown in this figure have been corrected for the channel-plate tilt.

2. Absolute energy calibration

Normalization of the silicon detector was achieved by using 8.78-MeV α particle emission from a ^{228}Th source mounted at the entrance to the GIC during calibration runs. In addition, a calibration run using beam was taken without gas in the GIC. The elastic peak position in this run (after correcting for energy losses in the target and foils as well as the pulse-height defect in the silicon stop detector[24]) gave a value for the beam energy using elastic kinematics. This value was 505±10 MeV.

3. Recoil detector position calibration

The position of the TLF in the recoil fragment detector was determined from the known position wire spacings which were visible in the data during calibration runs when a coincident signal from the PLF arm was not required. The absolute position normalization was obtained from the elastic recoil peak during normal data runs. The data runs at different detector angles were added together using weighting factors determined by the number of counts in the PLF arm. The continuity of the distributions of the parameters of interest for different recoil detector angles was verified for consistency.

4. Mass and charge calibrations

In the first approximation, the mass of the PLF's was formed for each event from the quantity $A_{\text{prelim}}=ET_{\text{CP}}^2$, where E is the total kinetic energy of the PLF and T_{CP} is the corrected time of flight (including an offset to account for differences in cable lengths) between the two channel

plates. This gives a series of mass peaks whose absolute positions still depend slightly on E and ΔE (or alternatively, nuclear charge) of the PLF's. Then for each event, the mass was formed by taking A_{prelim} and correcting it by a two-dimensional spline fit to the known positions of the mass peaks in E and ΔE. The resultant mass resolution full width at half maximum (Γ) was 0.9 mass units for elastically scattered ^{56}Fe and 0.75 for mass 52 (see Fig. 3).

The dependence of ΔE in the GIC on E, the kinetic energy of the PLF, was calculated for nuclear charges from 1 to 50 and from E/A from 0 to 10 MeV/nucleon using a phenomenological formula.[25] These values were given small corrections so that they would agree with the observed data from the GIC. A nuclear charge was then assigned to each event based on a linear interpolation between the nearest two ΔE values from charges at the value of E/A for that event. The nuclear charge determined in this way has a Γ resolution of 0.5 charge units, as shown in Fig. 4.

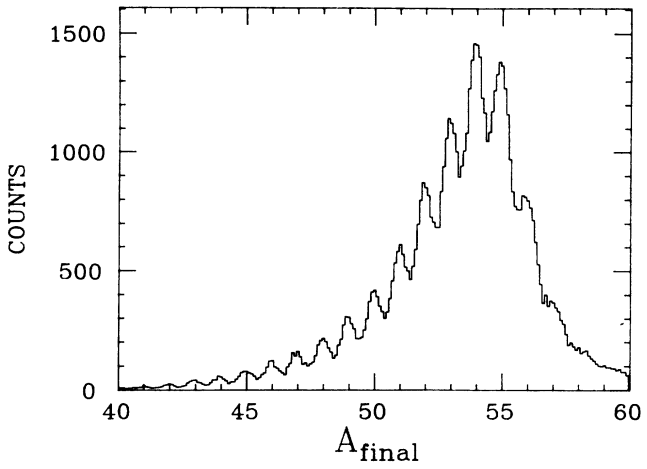

FIG. 3. The number of counts per bin as a function of the directly measured PLF mass (A_{final}). Only data which passed the criteria for analysis (see Sec. III B) and which had a TLF angle of less than 70° have been included, in order to exclude the elastic events.

B. Extraction of primary masses and excitation energies

1. Determination of primary mass

Since precompound emission of nucleons is negligable in the reaction under investigation,[1] the masses of the primary fragments (prior to particle evaporation) are fully determined by two-body kinematics from knowledge of the masses of the beam and target nuclei, the beam energy, the velocity of the PLF, and the scattering angles of both fragments. In general, the scattering angles and the PLF velocity will be changed randomly by evaporation, but the average value taken over a large number of similar events should not change, as long as nucleons are evaporated isotropically in the rest frames of the fragments. So then, in an average over a number of events with similar parameters, the primary reaction fragment masses are known[2–4] along with all the other kinematic parameters of the reaction including the total kinetic-energy loss (the amount of kinetic energy the reaction has transformed into internal energy of the nuclei). We have calculated the average *primary* PLF mass A_{PLF} by the equation, derived from nonrelativistic two-body kinematics,

$$A_{\text{PLF}}=\frac{A_P V_P}{V_{\text{PLF}}(\cos\theta_{\text{PLF}}+\sin\theta_{\text{PLF}}\cot\theta_{\text{TLF}})}\ , \tag{3.1}$$

where A_P ($\equiv 56$) is the projectile mass, V_P and V_{PLF} are the projectile and projectile-like fragment velocities, respectively, and θ_{PLF} and θ_{TLF} are the laboratory scattering angles of the PLF and TLF, respectively. The energy loss E_{loss} is calculated from the measured parameters by

$$E_{\text{loss}}=[(A_P+A_T)E'_{\text{PLF}}-E_P(A_T-A_{\text{PLF}})-2\cos\theta_{\text{PLF}}(E_P E'_{\text{PLF}} A_P A_{\text{PLF}})^{1/2}]/(A_P+A_T-A_{\text{PLF}})\ . \tag{3.2}$$

A_P and E_P are the mass and energy of the beam particles, A_T is the mass of the target nuclei, and E'_{PLF} is the PLF kinetic energy corrected for nucleon evaporation using the directly measured PLF mass A_{final} and the measured PLF kinetic energy $E_{\text{PLF}}^{\text{measured}}$,

$$E'_{\text{PLF}}=E_{\text{PLF}}^{\text{measured}}A_{\text{PLF}}/A_{\text{final}}\ . \tag{3.3}$$

Once the mass of the primary PLF (A_{PLF}) is known (on the average) and the mass of the PLF after evaporation has been measured, the amount of mass evaporated from the PLF, ΔA, can be calculated for each event,

$$\Delta A=A_{\text{PLF}}-A_{\text{final}}\ . \tag{3.4}$$

Figure 5 is a contour plot of ΔA versus the total kinetic-energy loss. The contours represent the number of counts. The island of data at relatively small energy losses and large evaporated mass is caused by scattering from the wire grid of the first channel-plate detector.

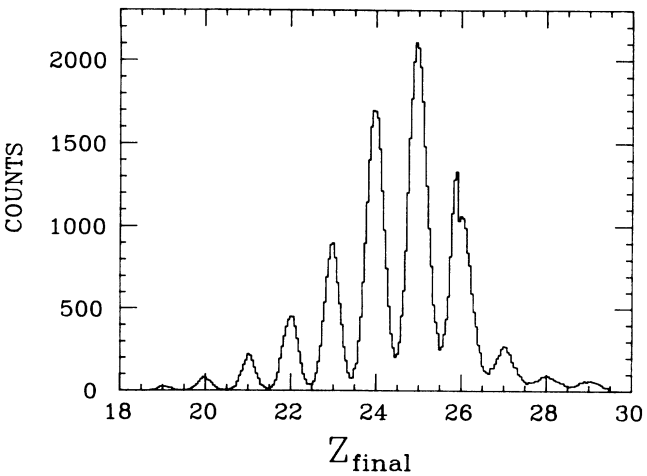

FIG. 4. Counts per bin as a function of measured PLF nuclear charge (Z_{final}). The same cuts in Fig. 3 have been used.

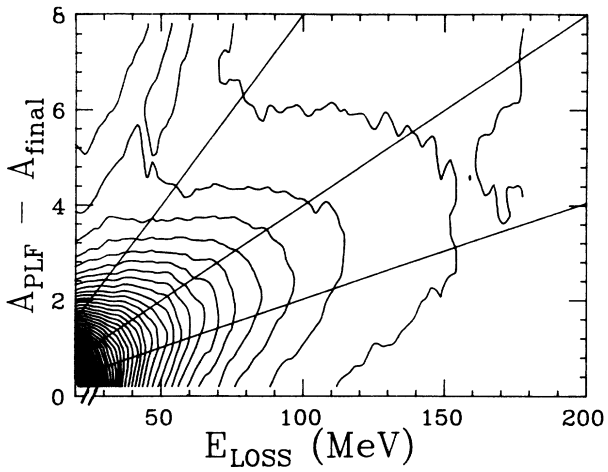

FIG. 5. Contour plot of counts as a function of energy loss (E_{loss}) and masses evaporated ($A_{PLF} - A_{final}$). The straight lines have been drawn to indicate the cases of (from top to bottom) TLF left in the ground state, equal division of excitation energy, and division proportional to projectile and target masses. In drawing these lines the ground-state Q values have been neglected and the assumption that every evaporated nucleon represents 12.5 MeV of excitation energy.

This scattering can be easily distinguished from the nonscattered data above an energy loss of 30 MeV.

A rough estimate of the excitation energy in the PLF can be obtained by assuming that each nucleon evaporated corresponds to 12.5 MeV of excitation energy E^*_{PLF}. As we will see later, this assumption leads to incorrect results, but nonetheless useful as long as they are not relied upon quantitatively. On the basis of this estimate and neglecting the energy required to form nuclear ground states (i.e., it is assumed that all of the energy loss not accounted for by PLF excitation is used in TLF excitation, $E_{loss} = E^*_{PLF} + E^*_{TLF}$), lines have been drawn which corresponds to, from top to bottom, (1) all excitation in the PLF, (2) excitation energy equally divided between PLF and TLF, and (3) excitation energy divided in the ratios of the fragment masses. Note that the data are concentrated between the two limits of energy conservation [(1) and the horizontal axis], all excitation residing in the PLF and all excitation residing in the TLF. Note also that most of the data lie in the region where the excitation energy is divided equally or according to the ratio of the fragment masses.

2. *Evaporation calculations*

In order to make a more accurate determination of the excitation energy, calculations of the evaporation process were performed using the PACE–2 code of Gavron.[26] This program uses a Monte Carlo technique to simulate the statistical emission of γ rays, neutrons, protons, and α particles. It has been used in a number of different ways, generally with good agreement with experiment.[11,27] The program's default values have been used. These have been found to give good agreement with experimental data in the regime of interest.[27] No discrete energy levels have been included in the calculations because most heavy ions have nearly continuous energy levels above the threshold for nucleon emission. It is also inappropriate to include discrete transitions which depend strongly upon the individual nuclide for any analysis in which initial mass and charge cannot be specified to a large degree of accuracy.

The initial parameters needed by PACE–2 correspond to properties of the nucleus prior to evaporation. These are the nuclear charge, mass, excitation energy, and spin. For spins less than about $20\hbar$, the output from this program changes very little as a function of spin. For this reason only an estimate of the spin given to the nucleus is needed. This was done by using the two limits of fusion and grazing, the former giving the maximum possible nuclear spin and the minimum impact parameter, and the latter giving no spin to the nuclei at the maximum impact parameter. Between these two limits the total angular momentum in the system and the amount transferred to the nuclei were found by a linear interpolation. The total angular momentum in the system was taken to be $L_{fusion} = 111\hbar$ at the fusion limit ($E_{loss} = 200$ MeV) and $L_{graz} = 255\hbar$ at the grazing limit ($E_{loss} = 0$).[28] The amount of this angular momentum transferred during the reaction during the reaction into PLF nuclear spin is zero at the grazing limit and L_{stick} at the fusion or sticking limit, where the system rotates as a solid piece (the nuclei have been assumed to be rigid spheres of radius proportional to $A^{1/3}$ for this limit). Linear interpolation between these limits gives the PLF spin,

$$L_{PLF} = (L_{stick}/L_{total})(E_{loss}/200\ \text{MeV}) \times [(L_{fusion} - L_{graz})(E_{loss}/200\ \text{MeV}) + L_{graz}] , \tag{3.5}$$

which is a parabola as a function of E_{loss} which passes through $L_{PLF} = 0$ when $E_{loss} = 0$. The value of E_{loss} in Eq. (3.5) has been taken to be twice the excitation energy of the PLF. This estimate agrees with experimental data for small to moderate energy losses[29,30] and is appropriate to use because of the relative insensitivity of PACE–2 at low spins. The actual angular momentum distribution given to PACE–2 was for three spins, $L = L_{PLF} - 1$, L_{PLF}, $L_{PLF} + 1$, where the proportion of nuclei having spin L is of the form $P(L) = (2L+1)/(6L_{PLF}+3)$. L_{PLF} is the nearest integer to the value calculated by Eq. (3.5), but it is not allowed to be less than $1\hbar$.

The evaporation of nucleons was calculated for elements from nuclear charges of 10 to 40, with eleven masses for each element centered on the most abundant isotope. For each initial charge and mass, a number of different excitation energies was also used as input. These were spaced at 10 MeV intervals for 0 MeV $< E_{loss} <$ 100 MeV and at 50 MeV intervals for 100 MeV $\leq E_{loss} \leq$ 200 MeV. The spin of the nucleus at each excitation energy was calculated as described previously in this section. With these input parameters, the decay chain of each charge, mass, excitation energy, and spin was calculated separately. The number of Monte Carlo cascades for each calculation was 1000. Two quantities were extracted,

$$\Delta A_{MC} = A_{PLF} - \langle A_{final} \rangle , \quad (3.6)$$

the average amount of mass lost during evaporation, and

$$\Delta Z_{MC} = Z_{PLF} - \langle Z_{final} \rangle , \quad (3.7)$$

the average amount of charge lost. The discontinuities caused by particle emission thresholds were smoothed by interpolating between no evaporation at $E_{loss}=0$ and the results of the calculation at $E_{loss}=18$ MeV. This step was taken to clean up the spectra at these low excitations. However, this interpolation means that this analysis is not valid for excitation energies below 20 MeV (any similar analysis based on nucleon evaporation could not be relied on in this region). Intermediate values of ΔA_{MC}, ΔZ_{MC} between the integer values of the initial parameters of A_{PLF}, Z_{PLF}, and E^*_{PLF} were found by a linear interpolation in these three dimensions.

The final result of these evaporation calculations can then be expressed as two functions, $\Delta A_{MC}(A_{PLF},Z_{PLF},E^*_{PLF})$ and $\Delta Z_{MC}(A_{PLF},Z_{PLF},E^*_{PLF})$. A_{PLF} and Z_{PLF} are the mass and charge, respectively, of the PLF prior to evaporation, and E^*_{PLF} is the PLF excitation energy. By definition, $\Delta A_{MC}(A_{PLF},Z_{PLF},0)=\Delta Z_{MC}(A_{PLF},Z_{PLF},0)=0$ for all values of Z_{PLF} and A_{PLF}. These functions are defined for all values of A_{PLF} and Z_{PLF} for $E^*_{PLF} \geq 0$. Values outside the range of calculations were found by extrapolation from the nearest two points. No data were used that gave final values outside the range of the calculations. This extrapolation was only used for the purposes of iteration. Emission of a γ ray would make no change in ΔA_{MC} or ΔZ_{MC}, but would decrease E^*_{PLF}. An α evaporation would increase both ΔA_{MC} and ΔZ_{MC}. The form of two of these functions is shown in Fig. 6 for $Z_{PLF}=26$ as a function of A_{PLF} and E^*_{PLF}. Notice that ΔA_{MC} is roughly independent of mass while ΔZ_{MC} is greater for proton-rich nuclei and

$$\Delta N_{MC} = \Delta A_{MC} - \Delta Z_{MC} \quad (3.8)$$

(the neutral mass evaporated) is larger for neutron rich nuclei. Evaporation increases with increasing E^*_{PLF}, approximately every 13 MeV yielding one evaporated mass, and nuclei with odd masses evaporate more easily than those with even masses. All of these qualitative features agree with expectations based on the neutron and proton binding energies.

3. *Event-by-event iteration analysis*

Earlier in this section it was shown how A_{PLF} (the average mass of the PLF before particle evaporation) could be determined from the kinematics in addition to the directly measured mass and charge of the PLF after evaporation, A_{final} and Z_{final}, respectively. The calculation of functions corresponding to the average evaporated mass and charge (ΔA_{MC} and ΔZ_{MC}) was also discussed. These pieces of information were combined in an analysis based on an iterative technique for finding the charge of the initial PLF, Z_{PLF}, and the PLF excitation energy E^*_{PLF}.

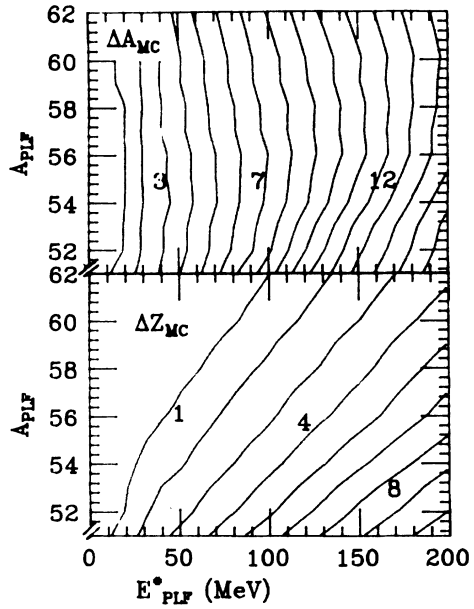

FIG. 6. Contour plots using calculated data from PACE-2 showing the number of masses evaporated (upper figure) and number of charges evaporated (lower figure) as a function of PLF initial excitation energy (E^*_{PLF}) and PLF initial mass (A_{PLF}), assuming $Z_{PLF}=26$. Each contour line corresponds to one evaporated mass or charge. Some of the contour lines are labeled with the number of units evaporated.

Given an initial charge Z_{PLF}, the value of E^*_{PLF} can be found unambiguously because A_{PLF} and A_{final}, and hence the value of $\Delta A_{MC}(A_{PLF},Z_{PLF},E^*_{PLF})$, are known. This conclusion assumes that ΔA_{MC} is a monotonic function of E^*_{PLF} for a fixed A_{PLF} and Z_{PLF}. This is true above the particle emission threshold. An additional piece of information provides the constraint,

$$\Delta Z_{MC}(A_{PLF},Z_{PLF},E^*_{PLF}) = Z_{PLF} - Z_{final} , \quad (3.9)$$

which limits the acceptable values for Z_{PLF}. An iteration was performed to find a self-consistent set of parameters A_{PLF}, Z_{PLF}, A_{final}, and Z_{final}, and E^*_{PLF} using the constraints imposed by the calculated functions ΔA and ΔZ and by the data. This iteration was performed on each event which was deemed acceptable by the following criteria: (i) A_{PLF} must be larger than or equal to A_{final}, (ii) Z_{final} must be between 2 and 40, and (iii) A_{final} must be between 2 and 100. These constraints were enforced so that the used data are in the range of the mass and charge calibrations and that the ΔA input into the iteration is

positive. Events violating type (i) are by far the most numerous of the rejected events and arise because of the uncertainty in A_{PLF} (and to a lesser extent in A_{final}) and scattering in the experimental apparatus.

Many of these scattered events were indistinguishable from the valid data if only the PLF data are considered. Figure 7 is a contour plot of PLF kinetic energy versus the TLF scattering angle. Several regions corresponding to different types of events are evident. The elastic events occur at the proper PLF kinetic energy and recoil angle (471 MeV and 72.7°, respectively), and the good events show a correlation between PLF kinetic energy and recoil angle. These good events lie in the region sloping down from the elastic toward smaller energies and angles. Random coincidences are in the region parallel to the recoil angle axis and elastic events rescattered in the experimental apparatus lie parallel to the PLF kinetic-energy axis. (The peak near 300 MeV originates from the 4% of elastically scattered particles which are degraded in energy in the acceleration wires of the channel-plate detector.[21]) After selecting only the "acceptable" events described above, only the region with good events and a short section of the scattered events near the elastic peak remain.

As the final step, the relevant quantities were binned into one-dimensional spectra, using only the events which passed criteria (i), (ii), and (iii). In the following discussion, the given quantities were extracted from a Gaussian fit on these distributions. The Gaussian fit provided the centroid, maximum height, and full width at half maximum (Γ), as well as probable errors associated with each quantity. The error bars on the following graphs have been determined from these probable errors.

The useful data from this analysis lie in the region 40 MeV $< E_{loss} <$ 200 MeV. The low E_{loss} data are excluded because of uncertainties in particle evaporation and the high E_{loss} data are left out because of low statistics. Events with PLF nuclear charges below 10 or above 32 are excluded because of the unreliability of the mass and charge calibrations for those data due to the very low cross sections.

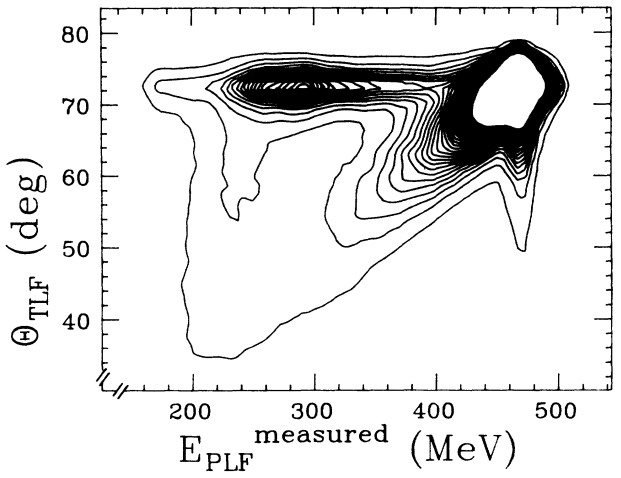

FIG. 7. Contour plot of counts as a function of measured PLF kinetic energy ($E_{PLF}^{measured}$) and TLF recoil angle (θ_{TLF}). The very highest contour lines near the elastic peak have been suppressed for clarity.

IV. RESULTS

A. Mass and charge distributions

Figure 8 shows the results for the mass [Fig. 8(a)] and the charge centroids [Fig. 8(b)] as well as the average of the neutron-to-proton number ratios (N/Z) [Fig. 8(c)] for the projectile-like fragments (PLF) as a function of energy loss. Pre- and post-evaporation data from this experiment are given as circles and squares, respectively (cf. Table I). Figure 8 shows, as observed in a previous[20] Fe + Ho experiment (lines in Fig. 8), that the average post-evaporation fragment mass and charge of the PLF's decrease with increasing energy loss (up to ~150 MeV), while the observed average N/Z ratio is nearly constant for up to 200 MeV of E_{loss}. The data show that the decrease in detected (post-evaporation) average mass is nearly entirely due to evaporation after the reaction: the pre-evaporation mass in Fig. 8(a) only decreases slightly with E_{loss}. This near constancy in average mass combined with the fast decrease in average PLF charge makes it not surprising that the average N/Z ratio for the PLF's increases dramatically with E_{loss} [Fig. 8(c)]. Note, however, that charge evaporation is not negligible in this reaction. It amounts to up to one unit at medium values of E_{loss}.

At energy losses above about 150 MeV all average A

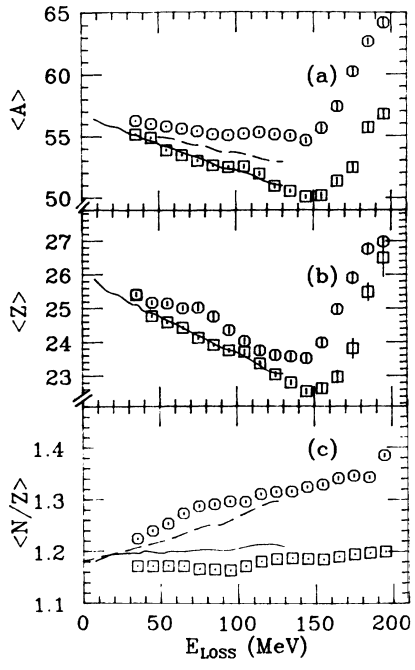

FIG. 8. The centroids of pre- (circles) and post- (squares) evaporation PLF masses (a), charges (b), and N/Z ratios (c) as a function of energy loss (E_{loss}). These data are compared with those of Breuer *et al.* (Ref. 20), where the dashed lines are the pre-evaporation data and the solid lines are the post-evaporation data.

TABLE I. Table of mass, charge, and N/Z centroids as a function of energy loss (E_{loss}). A_{PLF} and A_{final} are the pre- and post-evaporation PLF masses, respectively; Z_{PLF} and Z_{final} are the pre- and post-evaporation PLF nuclear charges, respectively; and $N/Z\mid_{PLF}$ and $N/Z\mid_{final}$ are the pre- and post-evaporation neutron to proton number ratios, respectively. ΔA is the centroid of the number of nucleons evaporated from the PLF and $\Delta A-\Delta Z$ is the number of neutrons evaporated.

E_{loss} (MeV)	$\langle A_{PLF}\rangle$	$\langle A_{final}\rangle$	$\langle Z_{PLF}\rangle$	$\langle Z_{final}\rangle$	$\langle N/Z\mid_{PLF}\rangle$	$\langle N/Z\mid_{final}\rangle$	$\langle \Delta A\rangle$	$\langle \Delta A-\Delta Z\rangle$
35	56.31±0.03	55.19±0.04	25.42±0.06	25.40±0.03	1.220±0.001	1.1718±0.0004	0.70±0.02	0.55±0.05
45	56.05±0.03	54.93±0.06	25.18±0.06	24.77±0.03	1.231±0.002	1.1720±0.0006	1.21±0.02	0.84±0.03
55	55.83±0.04	53.90±0.06	25.14±0.07	24.59±0.03	1.248±0.002	1.1723±0.0006	1.35±0.02	1.11±0.03
65	55.65±0.05	53.50±0.06	25.01±0.07	24.43±0.04	1.265±0.002	1.1723±0.0007	1.63±0.02	1.35±0.03
75	55.45±0.05	53.04±0.07	25.02±0.09	24.13±0.04	1.281±0.003	1.1669±0.0009	1.96±0.02	1.63±0.03
85	55.20±0.06	52.66±0.09	24.76±0.10	23.92±0.04	1.288±0.003	1.1664±0.0011	2.21±0.03	1.88±0.03
95	55.15±0.07	52.52±0.10	24.36±0.09	23.76±0.05	1.289±0.002	1.1651±0.0014	2.51±0.03	2.13±0.03
105	55.25±0.08	52.57±0.14	24.04±0.08	23.70±0.07	1.293±0.002	1.1731±0.0010	2.79±0.04	2.33±0.04
115	55.37±0.11	51.98±0.17	23.76±0.11	23.36±0.07	1.307±0.002	1.1821±0.0006	3.13±0.04	2.62±0.04
125	55.20±0.12	50.96±0.17	23.62±0.10	23.04±0.07	1.313±0.002	1.1866±0.0005	3.39±0.05	2.77±0.06
135	55.10±0.16	50.56±0.12	23.58±0.10	22.81±0.07	1.316±0.002	1.1885±0.0006	3.42±0.07	2.79±0.06
145	54.72±0.21	50.09±0.15	23.52±0.11	22.55±0.07	1.323±0.002	1.1870±0.0008	3.73±0.07	3.01±0.06
155	55.71±0.27	50.19±0.25	24.00±0.13	22.64±0.11	1.328±0.003	1.1862±0.0008	4.15±0.07	3.33±0.09
165	57.43±0.30	51.36±0.26	24.98±0.14	22.98±0.18	1.346±0.003	1.1912±0.0008	4.83±0.08	3.86±0.07
175	60.24±0.32	52.48±0.32	25.91±0.18	23.82±0.29	1.350±0.003	1.1957±0.0010	5.39±0.08	4.31±0.08
185	62.68±0.23	55.72±0.38	26.77±0.17	25.50±0.25	1.359±0.003	1.1984±0.0010	5.89±0.08	4.66±0.08
195	64.19±0.36	56.81±0.37	26.98±0.16	26.50±0.55	1.383±0.003	1.2006±0.0011	6.32±0.08	5.16±0.09

and Z values increase strongly. This is most likely due to a long interaction time component of the cross section where the effects of mass equilibration, the drift towards mass symmetry for projectile-like and target-like fragments, as predicted by the potential-energy surface,[20] start to become experimentally visible.

B. Excitation energies

As described in Sec. III B, the excitation energy of the projectile-like fragment (PLF) was derived using the evaporation calculation. The distribution of this excitation energy (E^*_{PLF}) as a function of energy loss (E_{loss}) is shown in Fig. 9(a). This plot also includes lines corresponding to three possible cases of excitation energy division. (For the purpose of these lines E_{loss} has been used to approximate the sum of the PLF and TLF excitation energies.) The upper line shows the case where all excitation energy resides in the PLF. The case where all excitation energy resides in the target-like fragment (TLF) is represented by the horizontal axis. The middle line shows where excitation energy is divided equally between the fragments, and the bottom line shows where the excitation energy is divided in the ratio $E^*_{PLF}/E^*_{TLF}=56/165$, i.e., proportional to the masses of the initial projectile and target. This last case is approximately equal to the case where the average fragment temperatures are equal. Notice that most of the data (aside from slit scattering, Sec. III) lie between the outermost lines.

The ratio of excitation energies (E^*_{PLF}/E^*_{total}) provides more information about the degree of equilibration than the absolute value of E^*_{PLF}. Figure 9(b) shows the ratio of the PLF excitation energy to the sum of the excitation energy in both fragments (E^*_{total}) as a function of energy loss. It is apparent that, as discussed in Sec. III B, the ratio is poorly defined at the lowest energy losses. In this representation, where also the ground-state Q values are properly taken into account, the lines of Fig. 9(a) become parallels to the E_{loss} axis, with lines of 1.0 and 0.5 and a band depending on PLF mass near 0.25. This figure indicates that not only are the majority of events to be found in the physical region $0\le E^*_{PLF}/E^*_{total}\le 1.0$, but also that a definite dependence of the most likely value on E_{loss} can be seen.

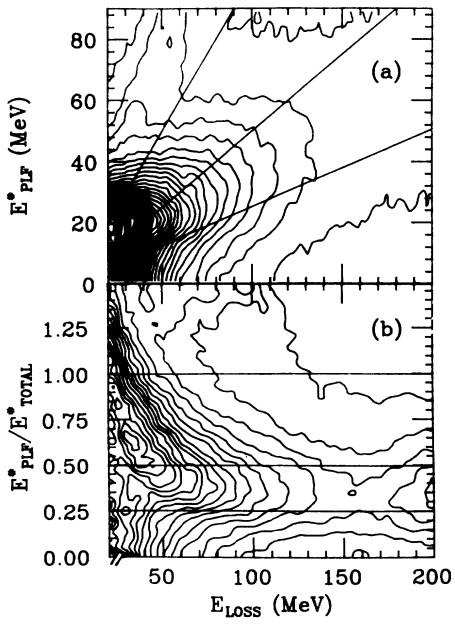

FIG. 9. Contour plots of counts as a function of energy loss and PLF excitation energy (E^*_{PLF}) (a) and E^*_{PLF}/E^*_{total} (b). The lines correspond to the same cases as the lines in Fig. 5.

By taking 10-MeV wide cuts on energy loss, the distribution of E^*_{PLF}/E^*_{total} can be investigated more quantitatively. A few representative cuts are shown in Fig. 10. This figure shows that for moderate E_{loss} values the distribution resembles a Gaussian, justifying the choice (Sec. III B) of fitting the distribution with a Gaussian function.

1. Excitation energy division centroids

Figure 11(a) is a plot of the centroids from the Gaussian fits of the peaks in the physically allowed region as a function of energy loss (circles in Fig. 11, see also Table II). The top line, located at $E^*_{PLF}/E^*_{total}=0.500$, on this figure corresponds to equal division of excitation energy between the fragments, and the lower line (at approximately $E^*_{PLF}/E^*_{total}=0.253$) shows the location where the average excitation energy would be divided in the ratio of the projectile and target masses (56/165). The error bars included are the probable errors of the centroid from the Gaussian fit. Systematic errors introduced by evaporation and the fitting procedure have not been included, but have been estimated by a Monte Carlo routine to be smaller than the statistical errors (see the Appendix).

One very striking feature of Fig. 11(a) is the observation that the centroids do not reach the ratio 0.25, even at very high energy losses of 170 MeV. One would expect the data to approach this value if temperature equilibrium were reached. Another feature of Fig. 11(a) is the indication that at the lowest energy losses, the excitation energy is nearly equally divided, while at larger energy losses, more energy resides in the heavier target-like fragment. This trend is similar to what one might expect from a model where the fragments have more equal temperatures at larger equilibration times.[31–33]

Because the relevant quantities are determined event-by-event, a number of different cases can be looked at. A good quantity to gate on is the pre-evaporation mass. This is related to the net mass transfer between the fragments. Figure 12 and Table III present the data by using mass bites for pre-evaporation PLF masses instead of averaging over all masses as in the previously presented data. The trend toward more unequal division at higher energy losses is still evident, but there is also a strong dependence on PLF mass. More massive PLF masses are correlated with more equal excitation energy division and vice versa. At first sight, the data in Figs. 12 and 11 appear to be inconsistent. Figure 11 shows a monotonic decrease in the excitation energy division ratio over the full range of E_{loss}, while in Fig. 12 one finds nearly constant values for the individual masses at intermediate E_{loss}. One has to realize, however, that Fig. 11 represents a cross-section weighted average over all masses. Thus the monotonically falling function in Fig. 11 is partially a reflection of the decrease in average projectile-like fragment mass, as observed in Fig. 8 below 150 MeV of E_{loss}.

Because the division of excitation energy seems to be roughly constant in the region between 100 and 150 MeV of energy loss, these data have been plotted in Fig. 13 as E^*_{PLF}/E^*_{total} versus pre-evaporation PLF mass. The upper line is equal excitation energy division and the lower one is excitation energy division proportional to the fragment masses. Figure 13 shows the dependence on net mass transfer even more strikingly than Fig. 12, indicating that the excitation energy division is roughly proportional to the net mass transfer and that fragments to which a greater net number of nucleons have been transferred have a greater fraction of the excitation ener-

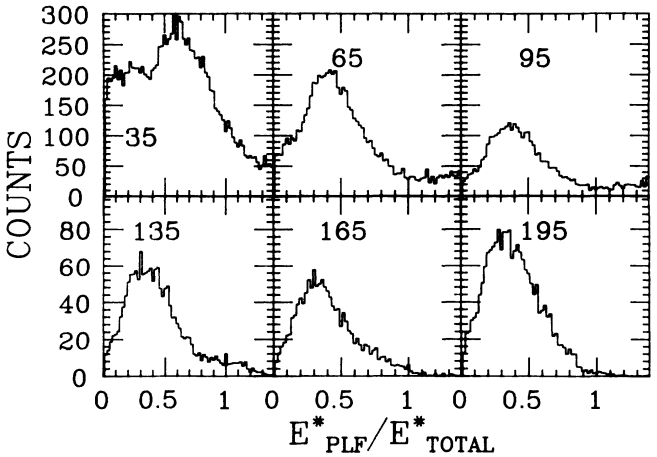

FIG. 10. Counts per bin as a function of excitation energy division (E^*_{PLF}/E^*_{total}) for different values of E_{loss}.

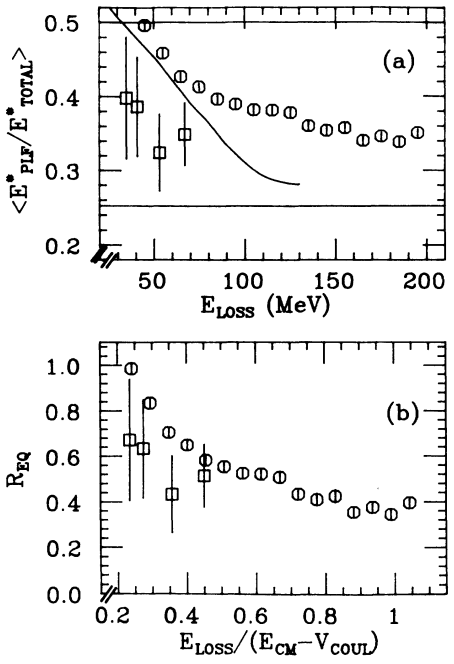

FIG. 11. Centroids of PLF excitation energy division (E^*_{PLF}/E^*_{total}) as a function of energy loss (a). The circles represent data from the present work; the squares are from Vandenbosch *et al.* (Ref. 8) and the line is from a calculation by Samaddar, De, and Krishan (Ref. 33). (b) shows the same data "corrected" for degree of equilibration [by plotting $R_{EQ}\equiv(E^*_{PLF}/E^*_{total}-A_P/A_{total})/(\frac{1}{2}-A_P/A_{total})$, where A_P is the projectile mass and A_{total} is the sum of the projectile and target masses, vs the fraction of available excitation energy, $E_{loss}/(E_{c.m.}-V_{Coul})$, where $E_{c.m.}$ is the center-of-mass energy of the reaction and V_{Coul} is the Coulomb barrier from Ref. 28].

TABLE II. Excitation energy parameters as a function of energy loss (E_{loss}). E^*_{PLF} and E^*_{TLF} are the excitation energies of the projectile-like and target-like fragments, respectively. E^*_{total} is the total amount of excitation energy in both fragments. Γ indicates that the full width at half maximum of the quantity in the parentheses is given. Both the raw width values and the values of the widths corrected for broadening introduced by the analysis method are displayed.

E_{loss} (MeV)	$\langle E^*_{PLF} \rangle$ (MeV)	$\langle E^*_{PLF}/E^*_{total} \rangle$	$\langle R_{E^*/A} \rangle$	$\Gamma(E^*_{PLF})$ (MeV) Uncorrected	Corrected	$\Gamma(E^*_{PLF}/E^*_{total})$ Uncorrected	Corrected
35	14.9±0.3	0.530±0.011	1.38±0.03			0.942±0.039	0.746
45	18.8±0.2	0.496±0.006	1.48±0.02	29.8±0.5	21.9	0.766±0.025	0.601
55	22.2±0.2	0.459±0.005	1.43±0.01	33.2±0.7	25.6	0.641±0.017	0.491
65	25.3±0.3	0.427±0.005	1.38±0.01	35.4±0.6	27.7	0.559±0.014	0.420
75	28.5±0.3	0.413±0.005	1.36±0.01	37.6±0.7	29.5	0.529±0.013	0.406
85	31.8±0.4	0.397±0.005	1.33±0.01	41.4±0.9	33.4	0.510±0.014	0.399
95	35.6±0.4	0.390±0.005	1.31±0.01	45.9±0.8	38.1	0.508±0.013	0.409
105	38.8±0.5	0.382±0.005	1.29±0.01	51.7±1.0	44.3	0.508±0.014	0.417
115	42.6±0.5	0.382±0.006	1.29±0.01	53.5±1.3	45.8	0.488±0.016	0.398
125	44.9±0.6	0.379±0.005	1.28±0.01	58.4±1.5	50.4	0.487±0.014	0.401
135	47.5±0.8	0.361±0.006	1.25±0.01	66.4±2.0	58.6	0.494±0.017	0.410
145	52.0±1.0	0.355±0.007	1.22±0.01	75.5±2.5	68.2	0.474±0.019	0.387
155	53.6±1.2	0.358±0.007	1.20±0.01	90.3±3.6	83.8	0.535±0.022	0.459
165	59.2±1.3	0.341±0.006	1.10±0.01	81.7±2.9	72.3	0.463±0.016	0.370
175	63.4±1.2	0.347±0.006	1.07±0.01	83.2±2.3	72.5	0.499±0.018	0.439
185	64.1±1.2	0.339±0.006	1.01±0.01	90.0±3.0	80.7	0.511±0.017	0.462
195	68.9±1.1	0.352±0.005	1.02±0.01	89.4±2.4	79.2	0.500±0.016	0.451

gy. (Or conversely, increasing mass loss from projectile-like fragments favors excitation energy division in the direction of the fragment mass ratios.) This feature agrees qualitatively with data from the quasi-elastic region.[9,10,15,16] Table IV shows E^*_{PLF}/E^*_{total} as a function of pre-evaporation PLF masses.

2. *Excitation energy widths*

In Sec. III B it was mentioned that the width of the Gaussian fit was extracted as well as its centroid. The width information is more difficult to interpret than the centroid data because the observed distributions are significantly broadened by recoil nucleus effects associated with evaporation. The experimental uncertainty in the directly measured quantities also adds to the observed widths.

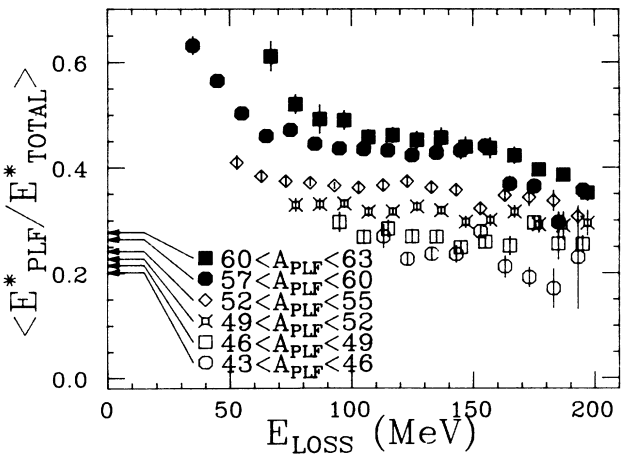

FIG. 12. Centroids of E^*_{PLF}/E^*_{total} as a function of kinetic-energy loss for different values of pre-evaporation PLF mass (A_{PLF}). The arrows represent the excitation energy division proportional to mass values for the different ranges of A_{PLF}.

A calculation of the various contributions to the widths of the raw distributions was done in order to apply a correction. This calculation includes the width added by evaporation recoil, microchannel plate timing resolution, TLF and PLF scattering angle resolution, the observed PLF mass resolution, the PLF kinetic energy resolution, and the correlation coefficient between the PLF velocity and TLF angle. The results from this calculation were subtracted in quadrature from the raw width values to give the corrected values. Figure 14(a) shows the full width at half maximum (Γ) of E^*_{PLF} as a function of energy loss for both the raw and corrected values. The error bars of the raw values are those deduced from the Gaussian fit, while the corrected values are given without error bars. The systematic error introduced by the correction is estimated to be 10% of the value. This figure shows, as expected, that the width of the excitation energy distribution increases with energy loss.

Similar to the situation for the excitation energy centroids, it is more instructive to investigate the width of the excitation energy distribution in relation to the total excitation energy available, specifically to consider the full width at half maximum of the excitation energy division [$\Gamma(E^*_{PLF}/E^*_{total})$]. Figure 14(b) shows this quantity (both raw and corrected values) as a function of energy loss. An interesting feature of this figure is that at the higher energy losses, this width becomes roughly constant and at the lower energy losses this width increases dramatically. The values in this figure are given in Table II. These values have *not* been corrected for the width introduced by averaging all the PLF masses together, rather than separating the individual masses.

To give some idea of the effect of this averaging, the

TABLE III. Centroids of PLF excitation energy division (E^*_{PLF}/E^*_{total}) as a function of energy loss (E_{loss}) and pre-evaporation PLF mass.

E_{loss} (MeV)	E^*_{PLF}/E^*_{total}					
	$43.0 \le A < 46.0$	$46.0 \le A < 49.0$	$49.0 \le A < 52.0$	$52.0 \le A < 55.0$	$57.0 \le A < 60.0$	$60.0 \le A < 63.0$
35					0.632±0.016	
45					0.565±0.008	
55				0.410±0.013	0.504±0.008	
65				0.384±0.008	0.461±0.010	0.612±0.028
75			0.330±0.012	0.375±0.007	0.472±0.008	0.521±0.017
85			0.331±0.010	0.372±0.006	0.446±0.007	0.493±0.027
95		0.297±0.018	0.332±0.007	0.366±0.005	0.437±0.008	0.491±0.018
105		0.269±0.013	0.317±0.009	0.362±0.008	0.436±0.009	0.459±0.013
115	0.270±0.021	0.285±0.015	0.317±0.006	0.367±0.008	0.433±0.009	0.463±0.014
125	0.227±0.010	0.270±0.013	0.326±0.009	0.374±0.009	0.424±0.009	0.453±0.015
135	0.237±0.013	0.269±0.012	0.320±0.006	0.362±0.008	0.429±0.010	0.457±0.018
145	0.236±0.016	0.249±0.011	0.297±0.010	0.357±0.007	0.433±0.016	0.440±0.018
155	0.280±0.012	0.259±0.011	0.301±0.010	0.323±0.012	0.441±0.013	0.437±0.019
165	0.213±0.020	0.252±0.017	0.316±0.011	0.347±0.011	0.369±0.013	0.423±0.015
175	0.192±0.019	0.296±0.012	0.292±0.015	0.343±0.016	0.364±0.013	0.396±0.009
185	0.171±0.036	0.256±0.029	0.290±0.026	0.337±0.019	0.297±0.019	0.386±0.013
195	0.230±0.097	0.255±0.015	0.295±0.023	0.308±0.014	0.357±0.012	0.352±0.014

quantity $\Gamma(E^*_{PLF}/E^*_{total})$ is plotted as a function of the pre-evaporation PLF mass A. This quantity, both raw and corrected for evaporation recoil and experimental resolution, is shown in Fig. 15, where a cut has been placed on 100 MeV $< E_{loss} <$ 150 MeV. This region was selected to be consistent with Fig. 13. The values in this figure, as in Fig. 13, tend to increase with increasing mass transfer to the PLF. This situation is not surprising because it is expected that the magnitude of the fluctuations in E^*_{PLF}/E^*_{total} would increase when the average of E^*_{PLF}/E^*_{total} increases.

V. DISCUSSION

A. Differences between the present and previous analyses

Earlier experiments[1-7] either measured the evaporated particles directly or measured both fragments in coincidence to deduce the primary masses, as in the present experiment or used a combination of the two. One of the experiments[1] used the same target-projectile system and a similar beam energy (8.5 MeV/A). The energies per nucleon of these experiments ranged between 5.1 and 8.5 MeV/A and used mass asymmetries in the range of $A_P/A_T = 0.31$ to 0.69. Almost all of these experiments[1-4,6,7] were interpreted to mean that the excitation energy was divided according to the ratio of the primary masses at all (except perhaps at the very smallest) energy losses.

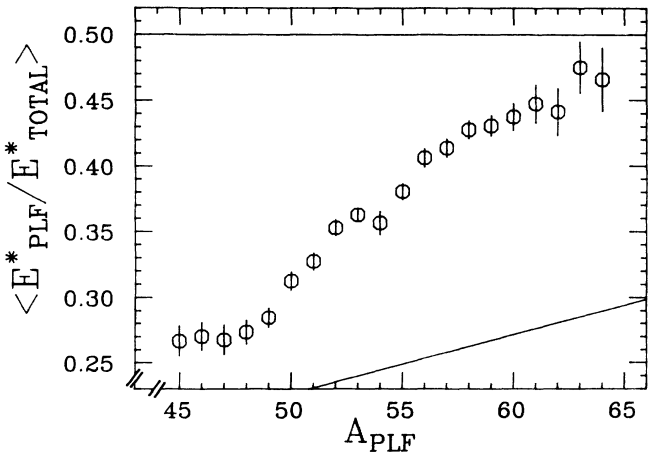

FIG. 13. E^*_{PLF}/E^*_{total} centroid as a function of pre-evaporation PLF mass (A_{PLF}) for 100 MeV $< E_{loss} <$ 150 MeV. The upper solid line represents equal division of excitation energy and the lower line represents division proportional to mass.

Later results, based on either using an evaporation code[9,10,11] or using mass asymmetry of fission fragments[8] (see Fig. 11), reached the conclusion that, at low to moderate energy losses, the amount of excitation energy per nucleon in the projectile-like fragment (PLF) is greater than that in the target-like fragment (TLF). In order to reconcile these two sets of experiments, we will compare our data with that of Hilscher *et al.*[1] This experiment was done using the same system and the slightly lower incident energy of 8.5 MeV/nucleon.

In Fig. 16, the directly measured neutron multiplicities from Ref. 1 are compared with the deduced multiplicities from the present analysis. The values are given in Table I. The circles represent the average number of nucleons evaporated from the PLF for a single event and the squares represent the average number of neutrons (the neutrons in evaporated alpha particles are also counted). This figure shows very good agreement between the neutron data and the present data, which indicates that not only has the total amount of evaporation been calculated correctly, but also suggests that the deduced amount of charged-particle evaporation is also correct. At the highest energy losses, the previous data and the present data begin to disagree significantly. This corresponds to the region where Hilscher *et al.* could not get their evaporation calculations to agree with the data. This discrepancy may be explained by the fact that at these en-

TABLE IV. PLF excitation energy (E^*_{PLF}/E^*_{total}) centroids and full width at half maximum (Γ) and fragment excitation energy per nucleon ratio ($R_{E^*/A}$) centroids as a function of pre-evaporation PLF masses (A_{PLF}). The range of energy loss has been restricted to be 100 MeV $< E_{loss} <$ 150 MeV.

	Centroid Values for 100 MeV $< E_{loss} <$ 150 MeV			
A_{PLF}	$\langle E^*_{PLF}/E^*_{total}\rangle$	$\langle R_{E^*/A}\rangle$	$\Gamma(E^*_{PLF}/E^*_{total})$ Uncorrected	$\Gamma(E^*_{PLF}/E^*_{total})$ Corrected
45	0.267±0.011		0.34±0.03	0.21
46	0.270±0.010	1.19±0.03	0.40±0.03	0.31
47	0.268±0.011	1.18±0.03	0.47±0.03	0.35
48	0.274±0.009	1.14±0.02	0.36±0.02	0.31
49	0.285±0.007	1.14±0.02	0.37±0.02	0.25
50	0.313±0.007	1.20±0.02	0.39±0.02	0.25
51	0.328±0.006	1.22±0.02	0.39±0.02	0.26
52	0.353±0.006	1.26±0.02	0.44±0.02	0.34
53	0.363±0.005	1.28±0.02	0.46±0.01	0.33
54	0.357±0.009	1.26±0.02	0.48±0.02	0.33
55	0.381±0.006	1.30±0.02	0.47±0.02	0.35
56	0.407±0.007	1.35±0.01	0.46±0.02	0.37
57	0.414±0.007	1.35±0.02	0.47±0.02	0.35
58	0.428±0.007	1.37±0.02	0.52±0.02	0.38
59	0.431±0.008	1.34±0.02	0.55±0.02	0.42
60	0.438±0.010	1.34±0.03	0.55±0.03	0.45
61	0.447±0.014	1.34±0.03	0.56±0.04	0.44
62	0.441±0.018	1.31±0.03	0.62±0.05	0.50
63	0.475±0.019	1.38±0.04	0.67±0.06	0.57
64	0.466±0.024	1.28±0.04	0.87±0.09	0.77

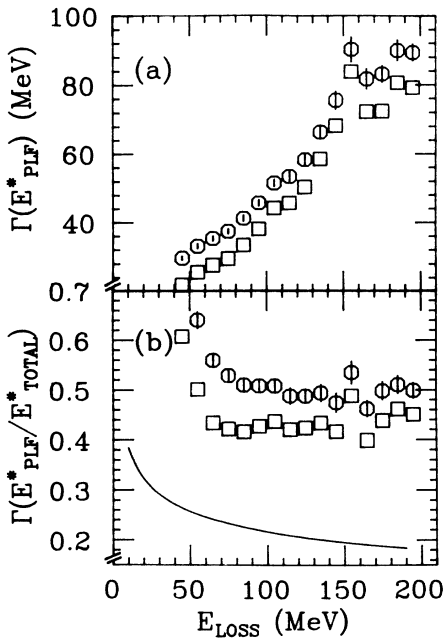

FIG. 14. (a) Full width at half maximum of the PLF excitation energy (E^*_{PLF}) as a function of E_{loss}. The circles are the uncorrected values and the squares are values which have been corrected for extra width introduced by the analysis method. (b) Full width at half maximum of the PLF excitation energy division (E^*_{PLF}/E^*_{total}) as a function of energy loss. The symbols correspond to those used in (a). The line represents a calculation of the width based on Morrissey and Moretto (Ref. 39).

ergy losses the previous experiment was close to the region where the maximum allowed amount of kinetic energy is transformed into excitation energy (166 MeV), while this region for the present data is somewhat higher (187 MeV).

Since Fig. 16 shows that (at least in the medium to low

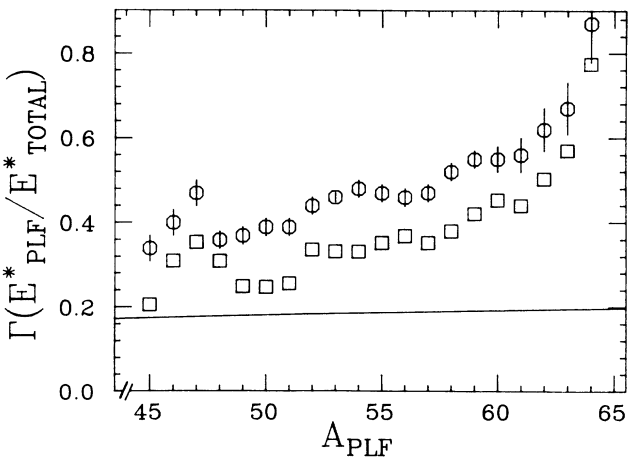

FIG. 15. The corrected full width at half maximum of the excitation energy ratio $\Gamma(E^*_{PLF}/E^*_{total})$ as a function of pre-evaporation PLF mass A_{PLF}. Only data between energy-loss values of 100 and 150 MeV have been included. The solid line is a calculation of the width based on Morrissey and Moretto (Ref. 39).

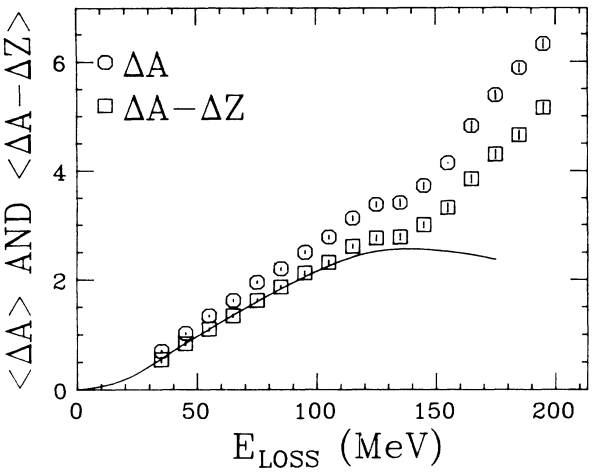

FIG. 16. Centroids of the number of masses (circles) and the number of neutrons [$\Delta A - \Delta Z$ (squares)] evaporated as a function of energy loss. The line is data from Hilscher *et al.* (Ref. 1) of the PLF neutron multiplicity.

energy loss range) the directly measured and the present derived neutron multiplicities agree, an explanation must be found for the disagreement between the conclusions drawn about the excitation energy division in these experiments. In Ref. 1 the PLF's were identified by charge only; it was assumed that the N/Z values of the fragment were given by the value of the total system. The number of evaporated particles from an excited nucleus is dependent not only on the amount of excitation energy in the nucleus, but also strongly on the charge-to-mass ratio[1,11,34] and the spin of the nucleus. After Ref. 1 was published an important feature of deep inelastic reactions was found, i.e., the equilibration of the charge-to-mass ratio is not complete for reactions that are not fully damped in energy [see Ref. 20 and the present N/Z data in Fig. 8(c)]. As Awes *et al.*[11] have pointed out, the assumption of equilibrated N/Z leads to the conclusion of equilibrated excitation energy, while the same data analyzed with knowledge about the behavior of the N/Z ratio give different results. Awes *et al.*[11] have reanalyzed the data of Ref. 1 and reached the conclusion that the excitation energy is not equilibrated until very large values of E_{loss}. As the energy loss increases, the primary TLF gets an increasingly larger number of protons. For a nucleus with a neutron excess, a smaller amount of excitation energy is necessary to evaporate a fixed number of neutrons than for a beta-stable nucleus. At medium to low energy losses, where the present data show that the fragment temperatures are not equal, the N/Z ratios for the fragments are found to be quite different from the assumptions of Ref. 1. Hilscher *et al.*[1] also took the slope parameters of the neutron distribution to give a measure of the temperature. Recently, difficulties with this assumption have been examined by Wile *et al.*[12]

An experiment was performed by Vandenbosch *et al.*[8] which measured the excitation energy division by using the mass distribution of fission fragments from the Fe + U system. This experiment did not have to use any assumptions about nucleon evaporation and so provides a measure of the excitation energy which is independent of most of the other experiments. Figure 11 includes the data of Ref. 8 which lie below the present data because of the greater mass asymmetry [$56/(56+238)=0.19$] in the input channel for that experiment. Aside from this difference, the data of Ref. 8 exhibit qualitatively the same features as the present results. An attempt to normalize the two data sets to account for different projectile-to-target mass asymmetries and different amounts of energy available for dissipation is done in Fig. 11(b). Here the range between "equal temperature" and "equal excitation energy" is covered by a scale of 0.0 to 1.0 and labeled

$$R_{\text{eq}}[\equiv(E^*_{\text{PLF}}/E^*_{\text{total}} - A_P/A_{\text{total}})/(\tfrac{1}{2} - A_P/A_{\text{total}})] .$$

The energy-loss scale of Fig. 11(a) has been converted by scaling according to the available energy above the Coulomb barrier. In this reference frame the Fe + Ho (circles) and the Fe + U (squares) data are compatible at the larger energy losses, but the Ref. 8 data is still too low at the smaller energy loss values, possibly indicating a faster equilibration in the system. Even though the scaling applied in Fig. 11(b) should not be taken quantitatively, the results emphasize the similarity of the excitation energy division in these two systems with strongly different methods of analysis.

The line on Fig. 11(a) corresponds to a calculation by Samaddar, De, and Krishan[33] using the nucleon exchange model for the case of 8.5 MeV/nucleon ^{56}Fe+^{165}Ho. While this calculation is qualitatively similar, it approaches the line of division according to mass much sooner than the present data.

It has already been shown that the present data agree qualitatively with recent experimental results (Fig. 11). In addition to these examples already given, another experiment by Sohlbach *et al.*[9] in the quasi-elastic region using the system ^{86}Kr+^{208}Pb has been done. This single arm experiment used an evaporation calculation to reconstruct the primary mass and excitation distributions. The data of Ref. 9 agree qualitatively with the present data in that both show a trend of excitation energy division in which the energy is distributed more equally at low E_{loss} and is shifted increasingly toward the TLF at higher E_{loss}. The two experiments also show that at a fixed energy loss, the fragment which accepts a net number of nucleons has a larger proportion of the available excitation energy (see Fig. 13). The present data indicate that these features previously observed[9] at very low energy losses actually persist over a very large range of energy loss until the reaction is nearly fully damped (Figs. 12 and 13).

The present experiment differs from the ones previously performed because a number of different techniques have been combined. The method of PLF-TLF kinematic coincidence is necessary to determine the mass of the primary fragments. If the directly measured mass of the PLF is added to this information, the number of evaporated nucleons is known, which gives data roughly comparable to measuring the evaporated particles directly. After these quantities have been formed, an evaporation calculation is used to extract excitation energies. To our knowledge this is the only experiment to combine

these three powerful techniques at once. The present data also have taken the primary N/Z ratio into account, as well as the possibility of evaporation of light particles other than neutrons.

B. Mass and charge distributions

An extensive study of the projectile-like fragment (PLF) mass and charge distributions from the $^{56}Fe+^{165}Ho$ reaction and 8.5 MeV/A has been reported previously.[20] However, the only directly available data were concerned with post-evaporation parameters. A comparison with the data of Breuer *et al.*[20] and the present data at 9.0 MeV/A is given in Fig. 8 for the average mass, charge, and N/Z ratio of the PLF's.

As can be seen in Figs. 8(a) and 8(b), the average post-evaporation mass and charge of the PLF's as a function of E_{loss} are nearly identical in both experiments. The data of Ref. 20 only extend to 130 MeV of E_{loss} due to the lower beam energy and much shorter data accumulation (lower statistics), thus a comparison with the high E_{loss} rise in average values is not possible. The data from Ref. 20 and from this experiment appear to disagree for the average N/Z ratio. However, two different quantities are plotted in Fig. 8(c). The solid line represents the ratio of the average neutron and average proton number, while the data points are the results for the average of the ratio of neutron and proton number for each fragment, i.e., $\langle N\rangle/\langle Z\rangle$ in contrast to $\langle N/Z\rangle$. These quantities are only identical in special cases. If one computes the ratios $\langle N\rangle/\langle Z\rangle$ from the values given in Table I for this experiment, one finds close agreement also in ratios of the average neutron to proton numbers between the two experiments. Figure 8(c) demonstrates the importance of a distinction between these quantities, while it also allows for a qualitative comparison between the two data sets.

Breuer *et al.*[20] attempted to estimate the pre-evaporation distribution centroids; their results are given as the dashed lines in Fig. 8. The previous experiment had no direct knowledge about the fragment excitation energy and had to rely on the assumption of equal temperature for nearly all E_{loss}. Figure 8(a) shows that the corrections for particle evaporation are only half of what is really needed, which also results in an underprediction of the ratio of the average neutron to average proton number.

The increase in average mass and charge at the highest E_{loss} seen in Figs. 8(a) and 8(b) was not observed in the previous experiment[20] due to insufficient data. At these high energy losses the reaction cross-section for this angle (26° in the laboratory system) has passed a minimum (cf. Fig. 9), most of the available kinetic energy is dissipated, and the reaction cross sections from positive- and negative-angle scattering ("orbiting") start to overlap. The reaction under investigation is known to exhibit orbiting characteristics as shown by Hoover *et al.*[19]

The interpretation of overlapping orbiting cross section is supported by results found for the same reaction at a 30° scattering angle (for which only fragmentary data exist). These larger angle data show an even more pronounced increase in average A and Z at identical energy losses, which would be expected if the fraction of the cross section due to orbiting dominates these increases (the nonorbiting part of the cross section is expected to fall off faster with absolute scattering angle than the orbiting one). The orbiting fraction of the cross section has presumably had a much longer interaction time, and thus has had more time for equilibration. Specifically, mass equilibration towards mass symmetry, for which a driving force is expected to exist from potential-energy surface calculations,[20] might finally become experimentally visible at interaction times equivalent to about a 50° revolution of the combined system.

C. Fragment temperatures

Feldmeier and Spangenberger[32] have published theoretical calculations for the $^{56}Fe+^{165}Ho$ system at 8.5 MeV/A, which should be directly comparable with the present data. However, the excitation energies were not calculated, but rather only the temperature ratios were presented. It has been mentioned in Sec. I that the excitation energy division between the fragments is related to the amount of temperature equilibration. The excitation energy is proportional to the fragment mass and the square of the temperature, $E^*=aT^2$ (a is the usual level density parameter). If the parameter a is assumed to be proportional to the fragment mass, then the square root of the ratio of the excitation energies per nucleon,

$$R_{E^*/A}=(E^*_{\text{PLF}}A_{\text{TLF}}/(E^*_{\text{total}}-E^*_{\text{PLF}})A_{\text{PLF}})^{1/2} \tag{5.1}$$

is the same as the ratio of the fragment temperatures $T_{\text{PLF}}/T_{\text{TLF}}$. The quantity $R_{E^*/A}$ was formed for each event according to Eq. (5.1). Though the distribution of this quantity is not a symmetric Gaussian, it was fit using the same procedure used for the other quantities. The centroids are presented in Fig. 17 and Table II. In contrast to the excitation energy division ratio, the excitation energy per nucleon ratio indicates that temperature equi-

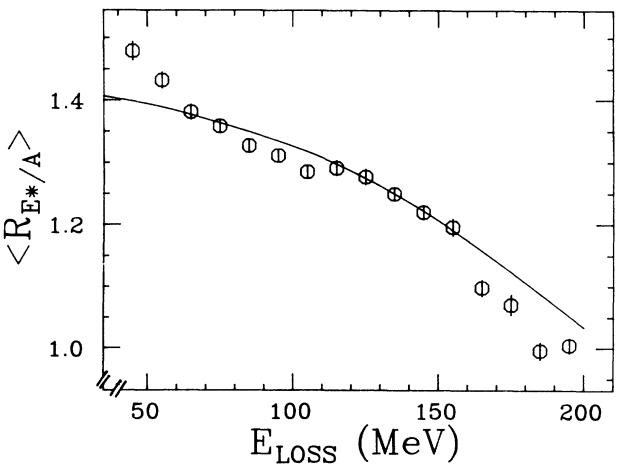

FIG. 17. Centroids of the ratio of the excitation energies per nucleon ($R_{E^*/A}$) as a function of energy loss. The line is a calculation by Feldmeier and Spangenberger (Ref. 32) of the temperature ratio ($T_{\text{PLF}}/T_{\text{TLF}}$).

librium is reached at the highest energy losses. The line on Fig. 17 shows the nucleon exchange model calculation of the ratio of fragment temperatures (T_{PLF}/T_{TLF}) by Feldmeier and Spangenberger[32] for the present system at 8.5 MeV/nucleon. We see good agreement over the range of the data.

The difference between the excitation energy ratio and the temperature ratio is not an inconsistency. The values of E^*_{PLF}/E^*_{total} presented do not take into account the different masses which went into the average (see Sec. IV B and the discussion of Fig. 12). The calculation of $R_{E^*/A}$, however, does include the event-by-event mass ratio. It should be recognized that because of the difference in level density parameters a between Fe and Ho, the scale of the temperature ratios presented here could be in error by an overall multiplicative factor.

The present data indicate that the equilibration of temperature is related to the mass exchange between the fragments. Moretto and Lanza[35] and Moretto[36] have suggested (and Schmidt[37] has elaborated), in order to explain the drift toward lighter projectile-like fragments, that the drive toward the smallest ground-state Q values is opposed by the drive to equalize temperatures. If this situation is an important process for damped reactions, then this may provide an explanation for the mass dependence shown in Fig. 13. It may also be the cause for the very slow drift toward equal fragment temperatures as seen in the present data. In other words, perhaps (at least for the strongly damped region) neither the ground-state Q value nor the temperature difference is minimized, and so the present data do not show either equal fragment temperatures or equal fragment masses. The nucleon-exchange model does not seem to show that this is the case. Both Samaddar and Feldmeier[32,33] have stated that this competition between statistics and energy is relatively unimportant for their calculations.

Brosa[38] suggests that the details of separation in the final phase of the interaction have a strong influence on the excitation energy division, since a large fraction of excitation energy is stored as deformation energy in the neck between the fragments. During the random rupture of the neck, the fragment which obtains the larger fraction of the neck obtains both an excess mass and a disproportionately large fraction of excitation energy from the neck deformation energy. This idea agrees with the observed strong mass dependence of excitation energy sharing (Figs. 12 and 13).

D. Excitation energy widths

The line on Fig. 14(b) is based on a formula given by Morrissey and Moretto[39] using the assumptions of equal fragment temperatures and Gaussian-distributed excitation energies. The formula used is

$$\Gamma(E^*_{PLF}/E^*_{total})^2 = 8\log(2)\frac{\sigma^2_{E^*_{PLF}}}{(E^*_{total})^2} = \frac{2T^3}{(E^*_{total})^2}\left[\frac{a_1 a_2}{a_1+a_2}\right]. \quad (5.2)$$

In this equation, T is the temperature of the system, and a_i ($i=1,2$) are the level density parameters of the fragments. For the purposes of this calculation, we have used $a_i = A_i/8$, where A_i is the fragment mass, and the average of the fragment temperatures for T. We see that while the shapes of the E_{loss} dependence of the calculation and the data are roughly the same, the magnitudes differ by about a factor of 2. It must be remembered, however, that this calculation assumes equal fragment temperatures, which is not correct for the region of the present excitation energy data.

Using Eq. (5.2) with $E^*_{total}=125$ MeV and $T=(8E^*_{total}/56+165)^{1/2}=2.1$ MeV gives the expected mass dependence of the width of the excitation energy division as the solid line in Fig. 15. Again note that Eq. (5.2) requires temperature equilibrium. For the lowest PLF masses, which are closest to thermal equilibrium (cf. Fig. 13) we also find the closest agreement between data and calculation. With increasing PLF mass both the temperature asymmetry (Fig. 13) and the discrepancy between calculation and data for the width increases (Fig. 15).

VI. SUMMARY

This paper has presented new information about the distribution of excitation energy between reaction partners in low-energy heavy-ion reactions. The mean values and widths of the projectile-like fragment excitation energy and the excitation energy division have been derived from measured values of the primary and secondary masses as a function of energy loss (between 40 and 200 MeV) and mass transfer for the 9.0 MeV/nucleon reaction involving $^{56}Fe+^{165}Ho$.

The present analysis has combined evaporation calculations, coincidence data, and mass and charge measurements explicitly. No assumption has been made about the distribution of the pre-evaporation mass, charge, and excitation energy. The determination of the pre-evaporation fragment masses was dependent on the assumption of a two-body final state followed by statistical emission. This assumption is mainly based on the data of Hilscher *et al.*[1] The post-evaporation mass and charge were measured directly in order to determine the amount of mass evaporated from the PLF. The PACE-2 evaporation code was used in this analysis to transform the measured quantities into PLF excitation energy. Every event was analyzed in this way, taking the N/Z ratio of the primary nucleus into account, as well as treating γ, neutron, proton, and α evaporation consistently. This analysis yielded results which agree with the directly measured neutron multiplicities of Hilscher *et al.*[1] The present method of analysis is limited by ambiguities from lack of nucleon evaporation at low values of energy loss and by the assumptions of statistical emission and two-body kinematics.

These results show that the relative amount of excitation energy in the PLF decreases as the energy loss increases, indicating that the fragment temperatures are more equilibrated at longer time scales. The case of excitation energy division according to the ratio of the frag-

ment masses is reached by the average value of the excitation energy division at $E_{\rm loss}=200$ MeV, which is the limit of the present data. This indicates that the excitation energy (like the charge) is not fully equilibrated until the reaction is nearly completely damped.

For a particular pre-evaporation mass, the division of excitation energy is approximately constant between 100 and 150 MeV of energy loss. It is also found that the excitation energy per nucleon of a fragment is strongly dependent upon the net mass transfer. The fragment accepting a net number of nucleons also has a larger amount of excitation energy than the average. This may be evidence for a correlation between nucleon and excitation energy exchange.

The results of the present experiment have extended and quantified the available knowledge about the distribution of excitation energy to nearly the full range of possible energy losses. These results have also taken the N/Z ratio into account explicitly in order to agree with the different types of experiments to measure the division of excitation energy. In addition the present paper has presented extensive excitation energy centroid and width data by which models of nuclear collisions in this region may be tested. The method employed can also be used for other systems so long as the assumptions of two-body kinematics and excitation energies significantly above the particle-emission threshold are still valid.

ACKNOWLEDGMENTS

The authors would like to thank R. J. McDonald, Harvey Styversrud, and the staff of the Lawrence Berkeley Laboratory Super-HILAC for their help, as well as J. Yurkon and W. G. Lynch for providing the parallel-plate avalanche counter used in this experiment. This work was supported by the U.S. Department of Energy and the National Science Foundation.

APPENDIX: Estimation of Possible Errors

The error bars in the figures shown in the present paper represent only the errors associated with the parameters extracted from the Gaussian fit. In addition to the statistical errors, there are also possible systematic errors associated with angle and energy straggling and evaporation recoil effects, and experimental resolution. In addition, the energy loss and PLF excitation energy, as derived from this analysis, may exhibit correlations which are a result of the analysis and which do not represent a physical relationship between these quantities. Hence, a Monte Carlo calculation was performed to simulate the effects of such processes.

1. Monte Carlo analysis

The input parameters for this Monte Carlo simulation were the PLF primary mass and charge $A_{\rm PLF}$ and $Z_{\rm PLF}$, respectively; the total available excitation energy $E^*_{\rm total}$; and the excitation energy division $E^*_{\rm PLF}/E^*_{\rm total}$. The post-evaporation PLF mass and charge were calculated from these input parameters by use of the matrices described in Sec. III B, $\Delta A_{\rm MC}(A_{\rm PLF},Z_{\rm PLF},E^*)$ and $\Delta Z_{\rm MC}(A_{\rm PLF},Z_{\rm PLF},E^*)$. The energy loss was calculated using the given total excitation energy and the ground-state Q value from the liquid drop model, i.e.,

$$E_{\rm loss}=E^*_{\rm total}-Q_{gg}(A_{\rm PLF},Z_{\rm PLF})\ . \tag{A1}$$

The PLF and TLF scattering angles were randomized over a Gaussian distribution to simulate evaporation recoil effects. The widths of this angle broadening were calculated from an approximation based on Refs. 1 and 40. These approximations are

$$\sigma_{\theta_{\rm PLF}}=(0.43^\circ)(A_{\rm PLF}-A_{\rm final})^{1/2}\ , \tag{A2}$$

$$\sigma_{\theta_{\rm TLF}}=(0.69^\circ)[(A_{\rm PLF}-A_{\rm final})(E^*_{\rm total}/E^*_{\rm PLF}-1)]^{1/2}\ ,$$

where $A_{\rm final}$ is the PLF mass after evaporation. Other quantities required by the analysis routine were also calculated. The kinetic energy of the PLF, E, was reduced by the factor $A_{\rm final}/A$ to account for the average kinetic energy carried away by evaporation. The PLF time of flight was calculated from $A_{\rm final}$ and the resultant reduced E. The parameters which correspond to the quantities directly measured in the experiment ($T_{\rm CP}$, $E_{\rm PLF}$, $\theta_{\rm PLF}$, $\theta_{\rm TLF}$, $A_{\rm final}$, and $Z_{\rm final}$) were analyzed by the same routine as the experimental data.

The results of this Monte Carlo calculation show that, aside from extreme cases (where $E^*_{\rm PLF}$ is below the particle emission threshold and where the ground state of the nuclide is very far away from stability), the systematic errors are smaller than the statistical errors. In addition it was shown that the width introduced by experimental resolution and evaporation recoil was the same for the Monte Carlo results and the correction applied to the data to within 25%.

2. Channel-plate efficiencies

The efficiency of the micro channel-plate detectors, which is, in general, a function of kinetic energy and nuclear charge,[41] was estimated from the data to follow approximately the function (for $Z_{\rm final}\geq 10$),

$$\epsilon\approx 0.67+0.0081Z_{\rm final}\ , \tag{A3}$$

where ϵ is the efficiency of the channel-plate system and $Z_{\rm final}$ is the nuclear charge of the PLF. This $Z_{\rm final}$ dependence increases the centroid of the Z distributions by 0.01 at 65 MeV and 0.04 at 130 MeV. Because this shift is less than the maximum allowed deviation of ΔZ from $Z_{\rm PLF}-Z_{\rm final}$ in the iteration procedure, the effect of the efficiency dependence on excitation energy quantities is negligible.

3. Effects of beam stability

Because of the size of the target, the maximum amount that the beam could be displaced is approximately 0.5 cm. This value would correspond to an error in the scattering angle of the PLF of 0.1° and an error in the angle of the TLF of between 0.5° and 1.0°. The larger error in the TLF angle is for the largest recoil angles. These

angular errors translate into errors of about 7–14 MeV in excitation energy. This possible error is greatest at the smallest values of E_{loss} because of the larger TLF angles and because of the smaller denominator in the ratio of interest E^*_{PLF}/E^*_{total}. For the same reasons, at the larger energy losses, the errors caused by beam steering decrease. Using the above values, the error in E^*_{PLF}/E^*_{total} at $E_{loss}=100$ MeV is about 10%. It should be noted that the values given in this section are for the worst possible (and highly unlikely) case in which the beam was always striking the target near the same edge. Target beam-burn patterns indicate that this was not the case. Also, our good agreement with the data of Hilscher *et al.* (Fig. 16) shows that such an effect did not significantly affect the data. The wandering of the beam over the face of the target and the beam spot size would give a maximum error to the width of the excitation energy division of about the same magnitude as the centroid (10%).

*Present address: Physics Department, Princeton University, Princeton, NJ 08544.

†Present address: Department of Physics, University of Manchester, Manchester, M13 9PL England.

[1]D. Hilscher, J. R. Birkelund, A. D. Hoover, W. U. Schröder, W. W. Wilcke, J. R. Huizenga, A. C. Mignerey, K. L. Wolf, H. F. Breuer, and V. E. Viola, Jr., Phys. Rev. C **20**, 576 (1979).

[2]R. Babinet, B. Cauvin, J. Girard, H. Nifenecker, B. Gatty, D. Guerreau, M. Lefort, and X. Tarrago, Nucl. Phys. **A296**, 160 (1978).

[3]B. Cauvin, R. C. Jared, P. Russo, R. P. Schmitt, R. Babinet, and L. G. Moretto, Nucl. Phys. **A301**, 511 (1978).

[4]Y. Eyal, A. Gavron, I. Tserruya, Z. Fraenkel, Y. Eisen, S. Wald, R. Bass, G. R. Gould, G. Kreyling, R. Renfordt, K. Stelzer, R. Zitzmann, A. Gobbi, U. Lynen, H. Stelzer, I. Rode, and R. Bock, Phys. Rev. Lett. **41**, 625 (1978).

[5]J. Péter, M. Berlanger, C. Ngô, B. Tamain, B. Lucas, C. Mazur, M. Ribrag, and C. Signarbieux, Z. Phys. A **283**, 413 (1977).

[6]B. Tamain, R. Chechik, H. Fuchs, F. Hanappe, M. Morjean, C. Ngô, J. Péter, M. Dakowski, B. Lucas, C. Mazur, M. Ribrag, and C. Signarbieux, Nucl. Phys. **A330**, 253 (1979).

[7]C. R. Gould, R. Bass, J. V. Czarnecki, V. Hartmann, K. Stelzer, R. Zitzmann, and Y. Eyal, Z. Phys. A **284**, 353 (1978).

[8]R. Vandenbosch, A. Lazzarini, D. Leach, D.-K. Lock, A. Ray, and A. Seamster, Phys. Rev. Lett. **52**, 1964 (1984).

[9]H. Sohlbach, H. Freiesleben, P. Braun-Munzinger, W. F. W. Schneider, D. Schüll, B. Kohlmeyer, M. Marinescu, and F. Pühlhofer, Phys. Lett. B **153**, 386 (1985); H. Sohlbach, H. Freiesleben, W. F. W. Schneider, D. Schüll, P. Braun-Munzinger, B. Kohlmeyer, M. Marinescu, and F. Pühlhofer, Nucl. Phys. **A467**, 349 (1987); H. Sohlbach, H. Freiesleben, W. F. W. Schneider, D. Schüll, B. Kohlmeyer, M. Marinescu, and F. Pühlhofer, Z. Phys. A **328**, 205 (1987).

[10]K. Siwek-Wilczynska, R. A. Blue, L. H. Harwood, R. M. Ronningen, H. Utsunomiya, J. Wilczynski, and D. J. Morrissey, Phys. Rev. C **32**, 1450 (1985).

[11]T. C. Awes, R. L. Ferguson, R. Novotny, F. E. Obenshain, F. Plasil, S. Pontoppidan, V. Rauch, G. R. Young, and H. Sann, Phys. Rev. Lett. **52**, 251 (1984).

[12]J. L. Wile, W. U. Schröder, J. R. Huizenga, and D. Hilscher, Phys. Rev. C **35**, 1608 (1987).

[13]L. G. Sobotka, G. J. Wozniak, R. J. McDonald, M. A. McMahan, R. J. Charity, L. G. Moretto, Z. H. Liu, F. S. Stephens, R. M. Diamond, M. A. Deleplanque, and A. J. Pacheco, Phys. Lett. B **175**, 27 (1986).

[14]H. Keller, B. Bellwied, K. Lützenkirchen, J. V. Kratz, W. Brüchle, H. Gäggler, K. J. Moody, M. Schädel, and G. Wirth, Z. Phys. A **328**, 255 (1987).

[15]H. R. Schmidt, S. B. Gazes, Y. Chan, R. Kamermans, and R. G. Stokstad, Phys. Lett. B **180**, 9 (1986).

[16]C. P. M. Van Engelen, E. A. Bakkum, R. J. Meijer, and R. Kamermans, Nucl. Phys. **A457**, 375 (1986).

[17]D. R. Benton, H. Breuer, F. Khazaie, K. Kwiatkowski, V. E. Viola, S. Bradley, A. C. Mignerey, A. P. Weston-Dawkes, and R. J. McDonald, Phys. Lett. **185B**, 326 (1987).

[18]D. R. Benton, Ph.D. thesis, University of Maryland, 1985 (unpublished).

[19]A. D. Hoover, J. R. Birkelund, D. Hilscher, W. U. Schröder, W. W. Wilcke, J. R. Huizenga, H. Breuer, A. C. Mignerey, V. E. Viola, Jr., and K. L. Wolf, Phys. Rev. C **25**, 256 (1982).

[20]H. Breuer, A. C. Mignerey, V. E. Viola, K. L. Wolf, J. R. Birkelund, D. Hilscher, J. R. Huizenga, W. U. Schröder, and W. W. Wilcke, Phys. Rev. C **28**, 1080 (1983).

[21]K. Kwiatkowski, V. E. Viola, Jr., W. G. Wilson, S. H. Zhou, and H. Breuer, Nucl. Instrum. Methods **225**, 65 (1984).

[22]G. Gabor, W. Schimmerling, D. Greiner, F. Bieser, and P. Lindstrom, Nucl. Instrum. Methods **130**, 65 (1975).

[23]H. Stelzer, Nucl. Instrum. Methods **133**, 409 (1976).

[24]S. Kaufman, E. Steinberg, B. Wilkins, J. Unik, A. Gorski, and M. Fluss, Nucl. Instrum. Methods **115**, 47 (1974).

[25]J. Ziegler, *Handbook of Stopping Cross-Sections for Energetic Ions in All Elements* (Pergamon, New York, 1980). The calculations were done using the program of T. C. Awes, Oak Ridge National Laboratory.

[26]A. Gavron, Phys. Rev. C **21**, 230 (1980).

[27]D.-K. Lock, R. Vandenbosch, and J. Randrup, Phys. Rev. C **31**, 1268 (1985).

[28]W. W. Wilcke, J. R. Birkelund, H. Wollersheim, A. D. Hoover, J. R. Huizenga, W. U. Schröder, and L. Tubbs, At. Data Nucl. Data Tables **25**, 529 (1980).

[29]J. C. Steckmeyer, F. Lefebvres, C. Le Brun, J. F. Lecolley, M. L'Haridon, A. Osmont, and J. P. Patry, Nucl. Phys. **A427**, 357 (1984).

[30]R. J. Puigh, P. Dyer, R. Vandenbosch, T. D. Thomas, L. Nunnelley, and M. S. Zisman, Phys. Lett. **86B**, 24 (1979).

[31]J. Randrup, Nucl. Phys. **A383**, 468 (1982).

[32]H. Feldmeier and H. Spangenberger, Nucl. Phys. **A428**, 223c (1984).

[33]S. K. Samaddar, J. N. De, and K. Krishan, Phys. Rev. C **31**, 1053 (1985).

[34]H. Breuer, N. R. Yoder, A. C. Mignerey, V. E. Viola, K. Kwiatkowski, and K. L. Wolf, Nucl. Instrum. Methods **204**, 419 (1983).

[35]L. G. Moretto and E. G. Lanza, Nucl. Phys. **A428**, 137c (1984).

[36]L. G. Moretto, Z. Phys. A **310**, 61 (1983).

[37]R. Schmidt, Z. Phys. A **320**, 413 (1985). R. Schmidt, Nucl. Phys. **A445**, 534 (1985).
[38]U. Brosa, Phys. Rev. C **32**, 1438 (1985) and private communication.
[39]D. J. Morrissey and L. G. Moretto, Phys. Rev. C **23**, 1835 (1981).
[40]R. Lide, Oak Ridge National Laboratory Report No. 3358, 1967 (unpublished).
[41]A. Gökmen, H. Breuer, A. C. Mignerey, B. G. Glagola, K. Kwiatkowski, and V. E. Viola, Jr., Phys. Rev. C **29**, 1595 (1984).